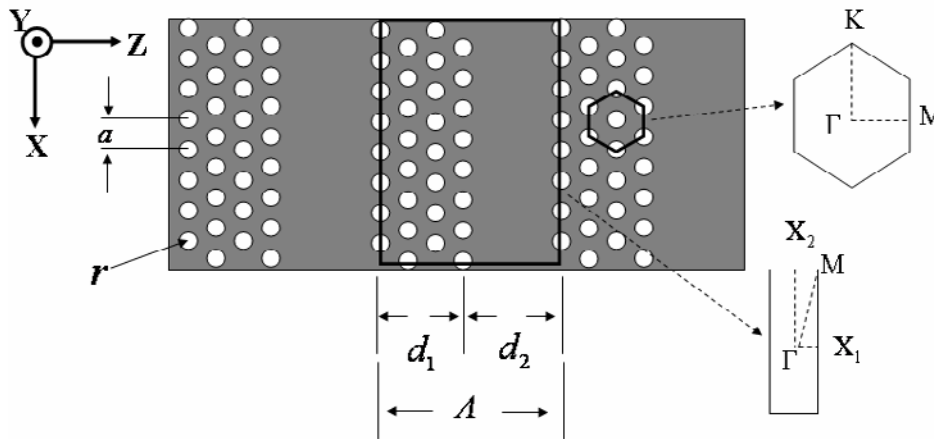


## Supplementary Information

**I. Schematic representation of the zero- $\bar{n}$  superlattices**

Schematic representation of a superlattice with 3 superperiods is shown in Fig. S1. The superlattice consists of alternating layers of hexagonal PhCs and homogeneous slabs. Note that the hexagonal PhC and the photonic superlattice have different symmetry properties, and therefore they also have different first Brillouin zones.



**Figure S1 | Schematic representation of the photonic superlattice.** There are two Brillouin zones defined as follows: one for the hexagonal photonic crystal lattice and one for the photonic superlattice.  $a$  is the lattice period and  $r$  is the radius of the holes forming the hexagonal lattice.  $d_1$  is the length of the PhC layer and  $d_2$  is the length of the PIM region.  $d_1 + d_2 = A$  is equal to the superperiod (SP) of the photonic superlattice.

**II. Effective indices from band diagram**

The effective refractive indices corresponding to the TM-like bands (Fig. S2b) are determined from the relation  $k=\omega|n|/c$  (with  $k$  in the first Brillouin zone) and plotted in Fig. S2c. Note that for the second band the effective index of refraction is negative since  $k$  decreases with  $\omega$  [23].

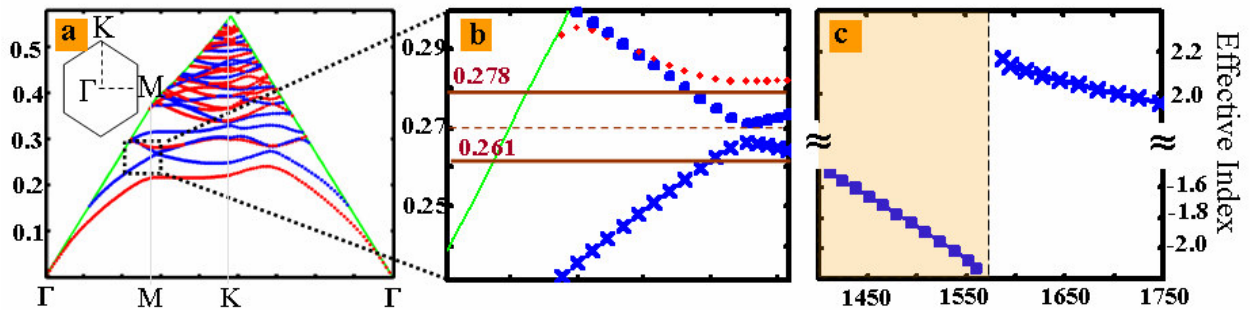


**Figure S2 | Band diagram of the PhC, a**, Band diagram of the PhC with the parameters given in Fig. 1. Inset: first Brillouin zone of the hexagonal PhC (for a schematic of the Brillouin zones, see the Supplementary Information, Fig. S1). The TM-like (TE-like) photonic bands are depicted in blue (red). The light cone is denoted by the green lines. **b**, A zoom-in of the spectral domain corresponding to experimental region of interest. Experiments were performed in the spectral region marked by the two horizontal lines (0.278-0.261 normalized frequency; 0.270 (dashed line) to 0.278 is negative index region). There is a complete TE-like band gap, and there are two TM-like bands. Lower frequency one band (marked with  $\times$ ) has positive effective index of refraction, higher frequency band (marked with  $\blacksquare$ ) has negative effective index of refraction. **c**, Calculated effective index of refraction of the PhC, corresponding to the two TM-like bands shown in Fig. S2b marked with the same symbols.

### III. Device modification for phase measurements, and theoretical calculations for interferometer transmission

Figure S3 shows a schematic representation of a device with 2 superperiods and the integrated Mach Zehnder Interferometer is modified after introducing the third superperiod. The adiabatic region remains unchanged if  $L_1$  is increased to  $L_1 + \Lambda$  and  $L_2$  is shortened by  $\Lambda/2$ , in both the input and output sides of the device. To keep the total length of the waveguide unchanged, the length  $L_3$  is increased to  $L_3 + \Lambda/2$ . This procedure is used each time a superperiod is added to the structure. In addition, to be able to compare devices with different number of unit cells in the PhC layer, a common reference point is used for all devices that have the same  $d_2/d_1$  ratio.

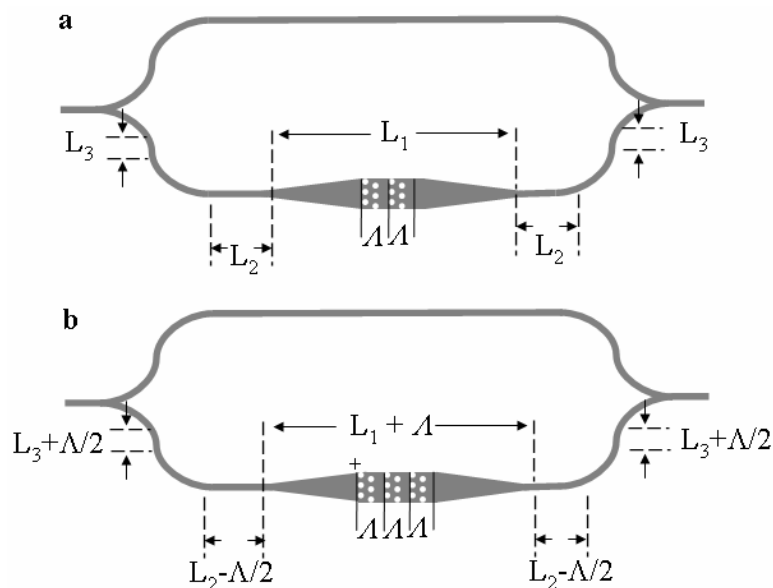


**Figure S3| Schematic representation of the device modification induced by adding a superperiod. a,** Integrated MZI of a device with 2 superperiods and a channel waveguide. **b,** Device modifications after the third superperiod is added. The length of the channel waveguide remains the same so as the effect of the additional superperiod is isolated.

In our implementation, the interferometer output intensity is given as:

$$I = I_1 + I_2 + 2\sqrt{I_1 I_2} \cos \phi \quad (\text{S1})$$

where  $\phi$  is the phase difference (or imbalance) between the modes propagating in the two arms (denoted by subscript 1 and 2). Considering our implementation, the phase  $\phi$  can be decomposed as:

$$\begin{aligned}\phi &= \phi_1 - \phi_2 = \frac{2\pi}{\lambda} \left[ (n_{wg} L_{wg\_1} + n_{slab\_1} L_{slab\_1} + n_{sl} L_{sl}) - n_{wg} L_{wg\_2} \right] \\ &= \frac{2\pi}{\lambda} \left[ n_{wg} (L_{wg\_1} - L_{wg\_2}) + n_{slab\_1} L_{slab\_1} \right] + \frac{2\pi}{\lambda} n_{sl} L_{sl}\end{aligned}\tag{S2}$$

where  $n_{wg}$ ,  $n_{slab\_1}$ ,  $n_{sl}$  are the effective mode refractive indices of the channel waveguide, the adiabatic slab in arm 1, and the zero-index superlattice, respectively.  $L_i$  denotes the corresponding lengths.

We note that the difference between the physical path length of the channel waveguides on both arms is designed to be equal to the physical path length of the tapering slab. Thus we have:

$$\begin{aligned}\cos[\phi] &= \cos \left[ \frac{2\pi}{\lambda} \left( (-n_{wg} L_{slab\_1} + n_{slab\_1} L_{slab\_1}) + n_{sl} L_{sl} \right) \right] \\ &= \cos \left[ \frac{2\pi}{\lambda} \left( (n_{slab\_1} - n_{wg}) L_{slab\_1} + n_{sl} L_{sl} \right) \right] \\ &= \cos[\phi_{slab\_wg} + \phi_{sl}]\end{aligned}\tag{S3}$$

The mode indices  $n_{wg}$ ,  $n_{slab\_1}$ ,  $n_{sl}$  have different frequency dispersion. We kept the phase ( $\phi_{slab\_wg}$ ), arising from  $\frac{2\pi}{\lambda} (n_{slab\_1} - n_{wg}) L_{slab\_1}$ , constant between different devices in each set of measurements by simply ensuring that the physical lengths and widths of the slabs are the same for each nanofabricated device. The remaining phase variation therefore is generated only by the photonic crystal superlattice ( $\phi_{sl} = \frac{2\pi}{\lambda} n_{sl} L_{sl}$ ). If  $n_{sl}$  is equal to zero,  $\phi_{sl}$  is zero too, hence the total phase difference  $\phi$  in the interferometer arises only from the  $\phi_{slab\_wg}$  component and is the same

for all the devices in each set. Therefore, the sinusoidal oscillations in the transmission and the free spectral range are determined only by  $\phi_{slab\_wg}$ .

#### IV. Experiments on tunability of the zero- $\bar{n}$ region

In order to demonstrate the tunable character of the zero- $\bar{n}$  bandgaps, we performed transmission experiments on four sets of binary superlattices, with each set having different superlattice ratios:  $d_2/d_1=0.74$  (Fig. S4a),  $d_2/d_1=0.76$  (Fig. S4b),  $d_2/d_1=0.78$  (Fig. S4d), and  $d_2/d_1=0.8$  (Fig. S4e). In all our experiments the negative index PhC has the same parameters as those given in the main text. Note that there is a slight ( $\sim 5\%$ ) change in  $r/a$ , which results in a small shift ( $<1\%$ ) in the spectrum. For example, Fig. 2c in the main text and Fig. S4d here correspond to the same design but there is about 10 nm ( $\sim 0.6\%$ ) shift in the center of the zero- $\bar{n}$  region. However, all the experimental data in this section corresponds to the same chip, therefore the invariance of the gap for the geometrical changes and its tunability can be clearly observed.

As described in the main text, each set of photonic superlattices consists of three devices of different period  $\Lambda$ , with the negative index PhC layer in the superlattice spanning 7, 9, and 11 unit cells along the  $z$ -axis, so that the thickness of this layer is  $d_1 = 3.5\sqrt{3} a$  (2.564  $\mu\text{m}$ ),  $d_1 = 4.5\sqrt{3} a$  (3.297  $\mu\text{m}$ ), and  $d_1 = 5.5\sqrt{3} a$  (4.029  $\mu\text{m}$ ), respectively. The corresponding thickness of the PIM layer is determined by requiring that the average index is zero [ $\bar{n} = (n_1 d_1 + n_2 d_2) / \Lambda = 0$ ], while keeping the ratio  $d_2/d_1$  unchanged for all devices in each set (see Table S1). Here,  $n_1$  and  $n_2$  are the effective mode indices in the PhC and homogeneous (PIM) layers, respectively, at the corresponding wavelength.

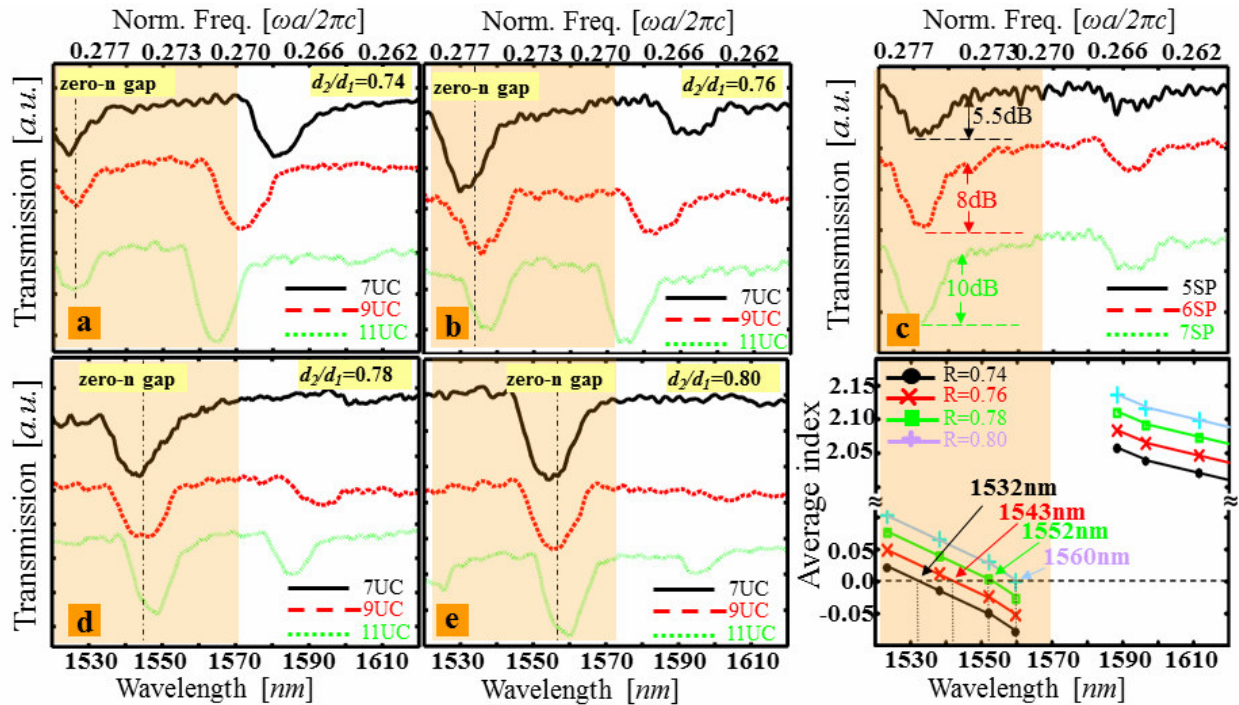
**Table S1 | Calculated parameters of the devices in the Fig. S4 (units in  $\mu\text{m}$ ).**

Fig. S4a			
# of unit cells	$d_1$	$d_2$	$A$
7	2.56	1.90	4.46
9	3.30	2.44	5.74
11	4.03	2.98	7.01
Fig. S4b			
# of unit cells	$d_1$	$d_2$	$A$
7	2.56	1.95	4.51
9	3.30	2.51	5.80
11	4.03	3.06	7.09
Fig. S4d			
# of unit cells	$d_1$	$d_2$	$A$
7	2.56	2.00	4.56
9	3.30	2.57	5.87
11	4.03	3.14	7.17
Fig. S4e			
# of unit cells	$d_1$	$d_2$	$A$
7	2.56	2.05	4.62
9	3.30	2.64	5.93
11	4.03	3.22	7.25

For the three devices in each set, we designed 7 SPs for the devices with 7 unit cells of PhC and 5 SPs for those with 9 and 11 unit cells of PhC (these designs ensure a sufficient signal-to-noise ratio for the transmission measurements). In these experiments we have tested both the existence of the zero- $\bar{n}$  bandgap as well as its tunability. For the three devices belonging to each set, we observed the zero- $\bar{n}$  bandgap at the same frequency whereas the spectral locations of the other bandgaps were observed to shift with the frequency – this confirms the zero- $\bar{n}$  bandgap does not depend on the superperiod length  $A$  (the gap existence is dependent only on the condition of path-averaged zero index:  $n_1d_1 + n_2d_2 = 0$ ) while the frequency of the regular 1D PhC Bragg bandgaps does depend on  $A$ . Our measurements show that the invariant, zero- $\bar{n}$ , bandgap is located at  $1525.5 \pm 1$  nm,  $1535.2 \pm 2$  nm,  $1546.3 \pm 1.5$  nm, and  $1556.5 \pm 2.5$  nm,

respectively (averaged over the three devices in each set). The slight red-shift with increasing number of unit cells in each set is due to effects of edge termination between the PhC and the homogeneous slab.

Furthermore, when we tuned the ratio  $d_2/d_1$  and repeated these same experiments we observed a redshift (see the values above) of the zero- $\bar{n}$  mid-gap frequency as we increased the ratio  $d_2/d_1$ . This result is explained by the fact that for the negative index band the refractive index of the 2D hexagonal PhC decreases with respect to the wavelength (see Fig. S2c) and therefore when the length of the PIM layer in the 1D binary superlattice increases (higher  $d_2/d_1$ ), the wavelength at which the effective index cancels is red-shifted. The effective index of the PIM layer,  $n_2$ , is calculated numerically and for the asymmetric TM slab waveguide mode corresponds to, for example, 2.671 at 1550 nm. By using these  $n_1$  (Fig. S2c) and  $n_2$  values, we determined the average refractive index for the different  $d_2/d_1$  ratios as summarized in Fig. S4f. A distinctive red-shift in the zero- $\bar{n}$  gap location is observed with increasing  $d_2/d_1$  ratios from the numerically modeling, demonstrating good agreement ( $\sim 0.5\%$  difference) with the experimental measurements (Fig. S4a, 4b, 4d, and 4e). Furthermore, Fig. S4c shows how the spectral features of the zero- $\bar{n}$  bandgap changes with increasing the number of superperiods. We note that this is the first rigorous and complete experimental confirmation of invariant and tunable character of zero- $\bar{n}$  bandgaps in photonic superlattices containing negative index PhCs.



**Figure S4 | Experimental verification of period-invariance and tunability of zero- $\bar{n}$  bandgaps.** **a**, Experimental verification of the zero- $\bar{n}$  bandgap in superlattices with varying period ( $A$ ). The ratio  $d_2/d_1=0.74$  and  $A=4.46 \mu\text{m}$  for black (solid),  $5.74 \mu\text{m}$  for red (dashed), and  $7.01 \mu\text{m}$  for green (dotted) curves (*a.u.* arbitrary units). **b**, Same as in **a**, but for  $d_2/d_1=0.76$ .  $A=4.51 \mu\text{m}$  for black (solid),  $5.80 \mu\text{m}$  for red (dashed), and  $7.09 \mu\text{m}$  for green (dotted) curves. **c**, Transmission spectra for superlattices with  $d_2/d_1=0.76$ , containing 5, 6, and 7 superperiods (SPs). Each PhC layer contains 7 unit cells ( $d_1=2.564 \mu\text{m}$ ,  $A=4.51\mu\text{m}$ ). **d**, Same as in **a**, but for  $d_2/d_1=0.78$ .  $A=4.56 \mu\text{m}$  for black (solid),  $5.87\mu\text{m}$  for red (dashed), and  $7.17 \mu\text{m}$  for green (dotted) curves. **e**, Same as in **a**, but for  $d_2/d_1=0.80$ .  $A=4.62 \mu\text{m}$  for black (solid),  $5.93 \mu\text{m}$  for red (dashed), and  $7.25 \mu\text{m}$  for green (dotted) curves. **f**, Calculated effective index of refraction for the superlattices with the ratios in **a**, **b**, **d**, and **e**. The wavelengths at which the average index of refraction cancels agree very well with the measured values.

## V. Near-field scanning optical microscopy and high-resolution imaging measurements

We further used near-field scanning optical microscopy (NSOM) to examine the zero- $\bar{n}$  transmission in the near-field, as illustrated in Fig. S5. Our NSOM is an aperture-type instrument, where the fiber is produced in National Chiao Tung University in Taiwan by using of thermal pulling method. A metal coating is used to create the aperture. The NSOM fiber was then attached to a tuning fork sensor produced by Veeco Instruments. The detection is performed with a New Focus 2153 InGaAs femtowatt photoreceiver with lock-in amplification. The NSOM instrument is a modified Veeco Aurora-3.

Coupling light into the zero- $\bar{n}$  superlattices is achieved by UV-curing adhesive bonding of a tapered lens fiber to the silicon input waveguide. The input fiber was stably UV-epoxy bonded to the devices selected for the measurements. We observed the light propagation through the sample by NSOM and used a widely tunable laser with controlled polarization to vary the input wavelength. From the near-field images of the superlattices (9 unit cells in PhC layer and  $d_2/d_1 \sim 0.76$ ), it can be seen that the light propagation in the superlattices is characterized by low transmission inside the zero- $\bar{n}$  gap (Fig. S5a,  $\lambda=1535$  nm), and high transmission outside the zero- $\bar{n}$  gap (Fig. S5b,  $\lambda=1560$  nm).

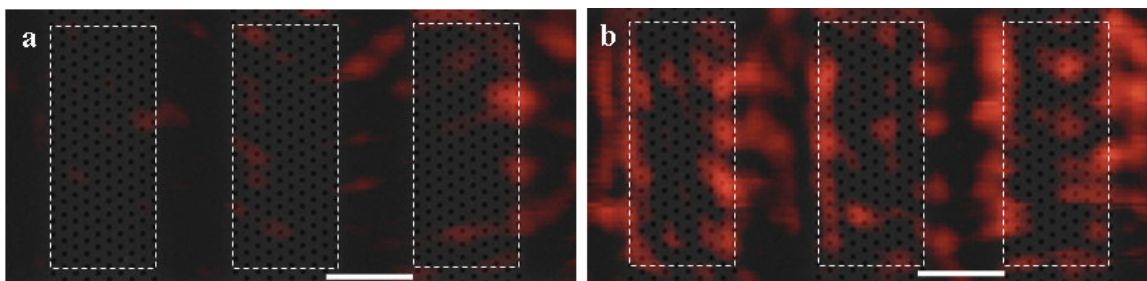


**Figure S5| Near-field scanning optical microscopy of zero- $\bar{n}$  superlattices. a,** Near-field image of a zero- $\bar{n}$  device that has 9 unit cells in each PhC layer at  $\lambda=1535$  nm (in the center of

the gap). **b**, Same as in **a** at  $\lambda=1560$  nm (in the high transmission). Scattering occurs at the edge of the PhC/PIM interfaces and is an indicative of transmission. Scale bar:  $2.5 \mu\text{m}$ .

In addition, we performed high spatial resolution imaging of the radiated input-output ports for the devices that have been used for the experiment presented in Fig.3c. Results are illustrated in the Fig S6 as follow: In the case of the reference arm (**i-iii**), we see light transmission for all three wavelengths, which corroborates the characteristics of the transmission spectrum in Fig. 3c. For the device arm (**iv-vi**) there is transmission for 1600 nm and 1530 nm but not for 1570 nm. This agrees with the transmission spectra in Fig. 3c. Note that although there is similar transmission for both arms at 1530 and 1600 nm, the interference output has 14dB difference.

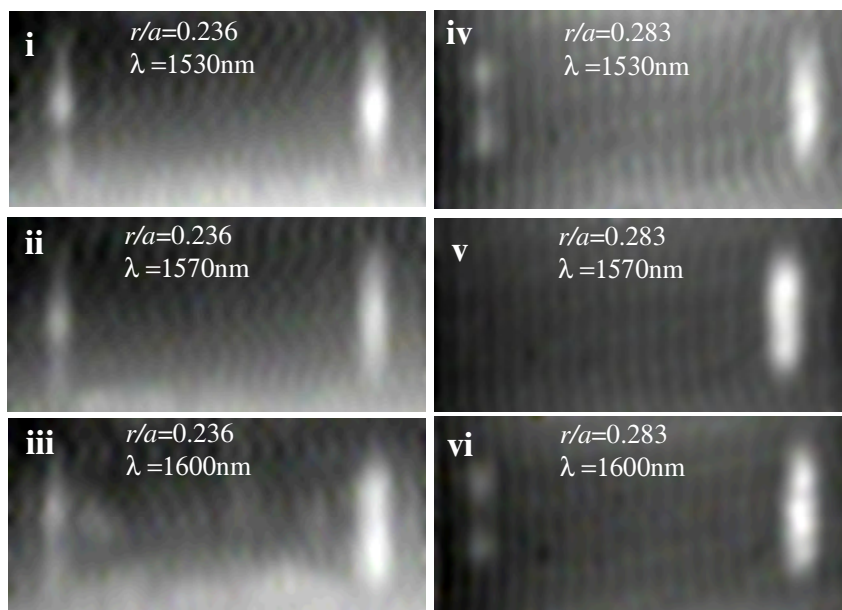


**Figure S6| Infrared images pertaining to the experiments corresponding to Fig3c. i-iii** is taken from the reference arm containing a PhC structure with  $r/a=0.236$  and **iv-vi** is taken from the device arm where the ratio  $r/a=0.283$ . In all the images the input beam is impinging onto the structure from the right, which means that light scattering at the left facet of the device indicates light transmission.

## VI. Computational study of the influence of disorder on the properties of zero- $\bar{n}$ superlattices.

In addition to the model for structural disorder of the photonic superlattice discussed in the paper, we have also considered two other disorder models in which either the radius of each hole in the PhC sections or the position of the holes is randomly perturbed. More exactly, the radius of the holes is set in the domain  $(r-\Delta r/2, r+\Delta r/2)$ , according to a uniform random distribution whereas in the second case the location of the holes is randomly perturbed by  $\Delta l$ . In these models, the degree of structural disorder is characterized by a disorder parameter defined as  $\sigma=\Delta r/r$  and  $\sigma=\Delta l/a$ , respectively. The main results of our computational investigations are summarized in Fig. S7. Thus, it can be seen that in the case of random perturbation of the radius of the holes the transmission spectra in the superlattice are only slightly affected, even if the disorder parameter is as large as  $\sigma=10\%$ . As observed, the main effect consists of a small decrease of the zero- $\bar{n}$  superlattice transmission with increasing values of the disorder parameter  $\sigma$ . It is seen, however, that structural disorder induced by randomly changing the location of the holes has a much larger effect on the transmission spectra. We note though that a value of  $\sigma=10\%$  corresponds to variations of tens of nanometers of the location of the holes, variations which are much larger than those measured in our fabricated devices.

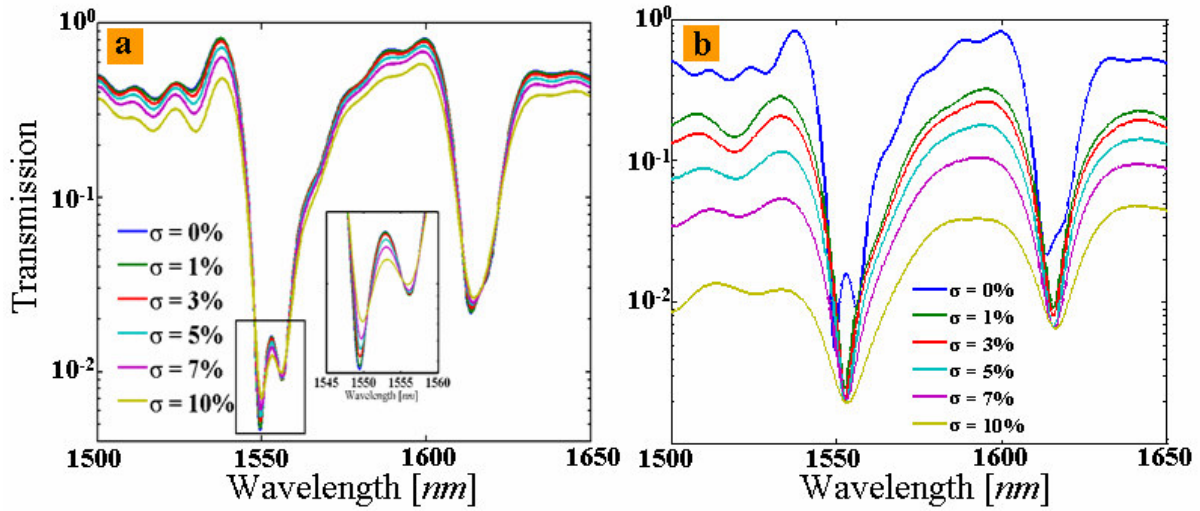


**Figure S7 | Transmission spectra calculated for different values of the disorder parameter  $\sigma$ .** The inset shows the expanded transmission spectra. **a**, The structural disorder is introduced by randomly changing the radius of the holes in the PhC sections of the superlattice. **b**, The structural disorder is generated by randomly perturbing the location of the holes.